Applied Surface Science 730 (2026) 166382

Contents lists available at ScienceDirect

Applied Surface Science

journal homepage: www.elsevier.com/locate/apsusc

Full Length Article

# Tribological performance improvement of titanium through laser-induced oxygen and nitrogen incorporation: experimental and molecular dynamics study

Amod Kashyap [a,b,*], Hendrik J. Ehrich [c,d], Manel Rodríguez Ripoll [c], Stefan J. Eder [c,d], Christian Greiner [a,b], Johannes Schneider [a,b]

[a] Institute for Applied Materials (IAM), Karlsruhe Institute of Technology (KIT), Karlsruhe 76131, Germany
[b] KIT IAM-ZM Micro-Tribology Centre (μTC), Karlsruhe Institute of Technology, Karlsruhe 76131, Germany
[c] AC2T Research GmbH, Wiener Neustadt 2700, Austria
[d] Institute for Engineering Design and Product Development, TU Wien, Vienna 1060, Austria

ARTICLE INFO

*Keywords:*
Surface engineering
Titanium
Microstructures
MD simulations
Adhesive wear

ABSTRACT

Titanium and its alloys have a pronounced tendency for adhesive wear and surface degradation under mechanical stress, severely limiting their widespread application in machine elements and components. A durable and efficient surface treatment for improving their wear resistance remains a major challenge. This study puts forward a cost-effective laser surface modification technique to enhance the tribological properties of commercially pure α-titanium (grade 1) by introducing interstitial oxygen and nitrogen. The process involves melting the titanium surface with a nanosecond pulsed laser in air, nitrogen, or argon atmosphere, followed by a smoothening step in argon atmosphere. Comprehensive characterisation using X-ray diffraction, electron microscopy, nanoindentation, and tribological testing reveals that interstitial oxygen and nitrogen significantly increase surface hardness and suppress adhesive wear by saturating titanium's valence bonds and reducing surface reactivity. The modified surfaces exhibit improved wear resistance and more stable friction behaviour under lubricated conditions, with minimal running-in and wear volume. The increased wear resistance has its origins at the atomic scale and is attributed to the role of oxygen and nitrogen occupying interstitial positions in the titanium lattice, as well as grain boundary deformation, as suggested by molecular dynamics simulations of nanoscratching. The merged experimental and computational approach establishes a solid foundation for tailored surface engineering strategies that optimise titanium's wear performance for future engineering applications.

## 1. Introduction

Titanium and its alloys are known widely for their exceptional strength-to-weight ratio, high–temperature stability, corrosion resistance, and biocompatibility, making them invaluable in aerospace, biomedical, and aerospace applications [1–6]. In aerospace, the high strength-to-weight ratio of titanium contributes to structural integrity and fuel efficiency, while its resistance to corrosion and its high-temperature stability ensure durability in harsh environments. The biocompatibility of titanium makes it an ideal choice for implants and prosthetics that interact with biological tissues without causing adverse reactions. Industrial applications leverage titanium's resistance to chemical attacks and mechanical fatigue, which are essential in environments where the equipment is subjected to high stress and other hostile conditions.

Although titanium has many advantageous properties, its widespread use is often hindered by its poor tribological performance. Titanium suffers from a high degree of adhesive wear in tribosystems due to the transfer of material to the countersurface [7,8]. This can result in increased friction, surface degradation, and, ultimately, equipment failure. Therefore, addressing these shortcomings is critical to the material's durability and functionality in various applications.

Surface engineering has played a vital role in improving the tribological performance of various materials. Surface modification

* Corresponding author at: Institute for Applied Materials (IAM), Karlsruhe Institute of Technology (KIT), Karlsruhe 76131, Germany.
*E-mail address:* amod.kashyap@kit.edu (A. Kashyap).

https://doi.org/10.1016/j.apsusc.2026.166382
Received 13 November 2025; Received in revised form 18 February 2026; Accepted 18 February 2026
Available online 19 February 2026

techniques include magnetron sputtering [9], oxidation [10], nitridation [7], etc. These techniques result in the formation of hard surface compounds, leading to an increase in wear resistance at the expense of a reduction in toughness and fatigue resistance. However, the surface hardening of titanium by incorporating oxygen and nitrogen atoms as interstitial solid solutions in the HCP α-titanium lattice is a very promising path to improve its tribological properties. Frederik et al. [8] annealed titanium in oxygen and nitrogen atmospheres, mentioning that oxygen and nitrogen atoms occupy the octahedral interstitial positions in the α-titanium lattice, resulting in a substantial increase in strength without degrading ductility and toughness. Kummel et al. [11] thermally oxidised Ti6Al4V samples and reported that there is a strong influence of interstitial oxygen on friction, amount of wear, and wear morphology. In a follow-up study, Kummel et al. [12] performed laser surface texturing on Ti6Al4V and found no significant effect of the texture topography on the tribological properties. However, the melt bulges containing interstitial oxygen and nitrogen were quite helpful in improving the tribological properties of Ti6Al4V.

Based on these findings, numerous studies have explored the effect of oxidised and nitrided surfaces on the mechanical and tribological properties of titanium and its alloys [13–17]. However, only a few studies are available to report the effect of interstitial nitrogen and oxygen on the microstructural evolution and tribological properties of titanium. The studies available till date offer unique perspectives on the mechanisms at play. Some attribute the effects to lattice expansion because of nitrogen and oxygen occupying interstitial positions [8,18], others focus on the orientation of slip planes [7], and some even explore the effect at the nano level and study the impact of grain size and the formation of nanotwins [19–22].

Beyond experimental and analytical approaches, numerical simulations have become increasingly important for understanding scratching and wear processes in titanium-based materials. Particle-based continuum methods such as the Material Point Method (MPM) have recently been applied to simulate scratch testing of titanium alloys with good agreement to finite element predictions and experimental load–displacement data [23]. However, such mesoscale approaches cannot resolve the underlying grain-scale mechanisms or the role of interstitial species on friction, deformation, and wear [24].

Therefore, it becomes imperative to independently study the effects of nitrogen and oxygen on the microstructural evolution and tribological properties of titanium. In the present study, we try to explore a cost-effective method to introduce oxygen and nitrogen into the interstitial positions of the titanium lattice. The surface of α-titanium was initially melted with the help of a nanosecond pulsed laser in three different atmospheres – air, argon, and nitrogen, to incorporate oxygen and nitrogen in the interstitial positions of the titanium lattice. Following this, a second laser treatment was applied in the presence of argon gas to smoothen the surface. The second smoothening step is advantageous in two ways: firstly, it provides an optimum surface roughness for application in aerospace components, and secondly, it removes the cracks caused by the addition of nitrogen and oxygen in the titanium matrix [25]. Afterwards, we studied the influence of interstitial oxygen and nitrogen on the microstructural evolution and tribological behaviour using various advanced characterisation techniques. We complement these efforts by performing molecular dynamics (MD) simulations of scratching nanocrystalline Ti and sub-stoichiometric TiN ($TiN_{0.3}$) surfaces, which serve to provide a detailed atomistic insight into the effects of nitrogen incorporation and microstructure on local deformation and contact mechanics.

## 2. Materials and methods

Commercially pure α-titanium (Ti) grade 1 was bought from ARA-T (Dinslaken, Germany) and cut into 25 mm × 8 mm discs. The discs were ground to an average surface roughness of $S_a \approx 450$ nm with a diamond wheel of grit D91.

### 2.1. Laser surface modification

The laser surface modification was conducted using a Piranha II marking laser system (ACSYS, Kornwestheim, Germany) with a maximum power output of 20 W. The laser source was an Yb-doped glass fiber laser, SPI G4 Z-Series EP (Southampton, United Kingdom), operating at a wavelength of 1060 nm. The laser spot was guided across the surface by a Scanlab SCANcube 10 (Scanlab, Puchheim, Germany) galvanometer scanner, and a 100 mm focal length F-theta lens (Linos, Göttingen, Germany) was employed for focusing. The laser system is capable of operating in both pulsed and continuous wave (CW) modes. In pulsed mode, high peak power can result in rapid melting and partial vaporisation of the surface, which facilitates efficient material removal but can also increase the formation of keyholes and surface cracks. In contrast, the CW mode provides lower peak power over a longer duration, leading to almost exclusively surface melting with significantly less vaporisation. While pulsed mode was selected for the melting step, the smoothing step was performed under CW mode due to its ability to minimise metal vaporisation and reduce defect formation. The nanosecond pulsed Yb fiber laser was selected for the melting step because its high peak power and short interaction time enable efficient melting and rapid solidification with a relatively shallow heat affected zone, while remaining compatible with standard industrial marking systems, thus preserving process simplicity and cost efficiency. Laser parameters are provided in Table 1; these parameters are based on the previous study done by Kummel et. al. [18]. Although a detailed parameter study is outside the scope of this paper, it should be noted that variations in laser settings led to the formation of keyholes and surface cracks during the smoothing process. The laser surface modification was conducted in the following steps (a schematic representation of the process can also be found in Fig. 1):

1. Melting of the surface with nanosecond pulses in air, nitrogen and argon atmosphere by closed packing laser tracks. The surface melting was done at a packing density of 200 % with an overlap of 50 % so that no channel textures were visible.
2. Smoothening of the surface in continuous wave mode of the laser in argon atmosphere perpendicular to the melting step with an overlap of about 83 %

The average surface roughness of the samples produced under the three different environmental conditions (air, nitrogen, and argon) ranged from $S_a \approx 350$ nm to 400 nm. The surface melted under an argon atmosphere had a metallic shiny appearance, while the surfaces melted under air and nitrogen had a ceramic-like appearance and were matte.

**Table 1**
Parameters for laser surface modification according to [18].

| Parameters | First laser process (melting) | Second laser process (smoothening) |
|---|---|---|
| Laser mode | Pulsed | Continuous wave |
| Nominal laser power (W) | 9.1 | 10 |
| Pulse length (ns) | 26 | – |
| Pulse energy (mJ) | 0.091 | – |
| Average energy density/ Fluence (J/cm$^2$) | 8.8 | – |
| Average power density/ Irradiance (W/cm$^2$) | – | $0.45 \times 10^6$ |
| Pulse repetition rate (kHz) | 100 | 20 |
| Scan speed (mm/s) | 362 | 62 |
| Pulse spacing (μm) | 3.62 | – |
| Track spacing (μm) | 15 | 5 |
| Process repetitions (–) | 2 | 2 |
| Packing density (%) | 200 | 600 |
| Atmosphere | Air, nitrogen, argon | Argon |

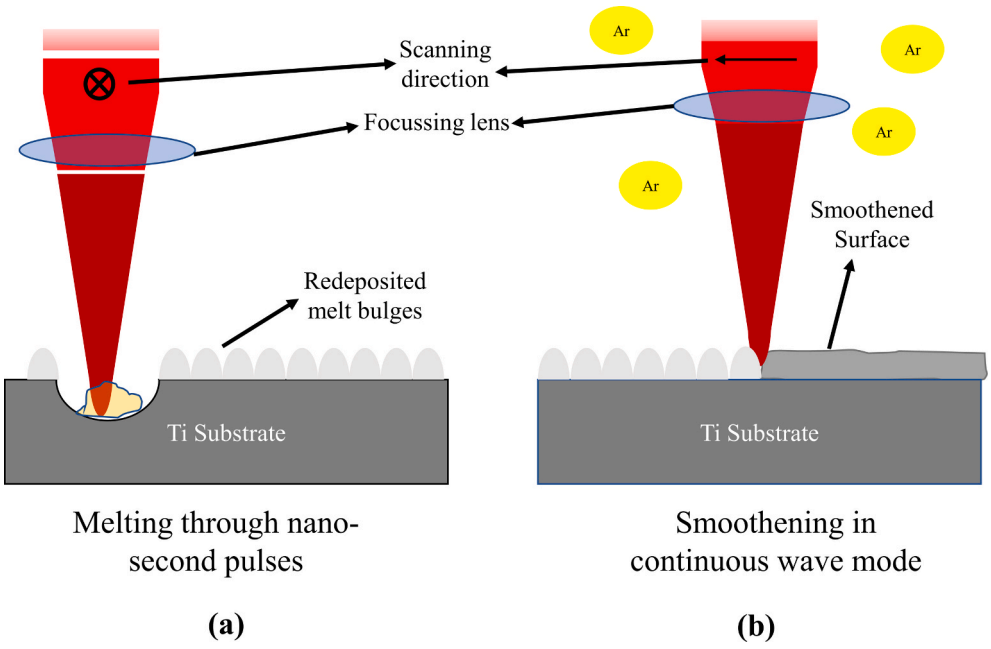


**Fig. 1.** Schematic diagram of laser surface modification (a) melting of Ti substrate with nano-second pulses, (b) smoothening the melt bulges with the continuous wave mode of the laser [18].

### 2.2. X-ray diffraction

X-ray diffraction analyses were performed using a 4-circle diffractometer and Fe-filtered Co Kα radiation (wavelength $\lambda = 1.79$ Å). A pinhole collimator with a nominal diameter of 1 mm was used as the primary aperture and a secondary slit aperture of $2\theta = 0.8°$ in front of a scintillation counter. A $2\theta$ range from 30° to 160° was scanned with a step size of 0.025°. In order to exclude possible influences of crystallographic texture on the qualitative phase analysis, the diffractograms were determined for several sample tilts around the polar axis $\psi$. The tilts were varied within a range of $0 < \psi < 60°$, whereas the tilts are equally distributed over $\sin^2\psi$.

### 2.3. Electron microscopy

The microstructure was analysed by dual-beam focused ion beam (FIB), scanning electron microscope (SEM) (Helios NanoLab Dualbeam 650, ThermoFisher, Hillsboro, USA). Thin lamellas for transmission electron microscopy were prepared by cutting the cross-sections and thinning them by FIB. Before the cutting process, two layers of platinum were deposited on the surface of the sample to protect it from ion damage. Immersion mode was used to analyse the microstructures. Images were also taken in scanning tunnelling electron microscope (STEM) mode of the SEM after preparing the lamellas to better understand the microstructures.

### 2.4. Nanoindentation

Nanoindents were performed on a Hysitron TI 950 Triboindenter (Minneapolis, USA) equipped with a modified Berkovich indenter tip. The samples were embedded in a polymeric resin, and metallographic cross-sections were prepared for all the samples by grinding them down to 4000 grit SiC paper and subsequent polishing with 6 µm, 3 µm and 1 µm diamond paste. Afterwards, a final mechanical-chemical polishing step was done using a mixture of 90 ml OP-U solution and 10 ml 30 % $H_2O_2$. A load of 10 mN was applied, and a total of 50 indentations were performed across the cross-section of each sample in the laser-modified zone. The hardness and the reduced elastic modulus values were calculated using the method proposed by Oliver and Pharr [26].

### 2.5. Tribological testing and analysis

An Optimol SRV II tribometer (Optimol Instruments, Munich, Germany) was used in a reciprocating sliding mode perpendicular to the direction of the first melting step in the laser modification process. Cylindrical counter bodies of 10 mm × 10 mm made from 100Cr6 steel (SKF, Schweinfurt, Germany), with a roughness of 0.15 µm, were used. The counter bodies were arranged with their cylinder axis parallel to the surface and at an angle of 5° to the sliding direction. The normal load of 20 N (resulting in a maximum Hertzian contact pressure of around 110 MPa), frequency 20 Hz, stroke length of 0.2 mm, and a total test duration of 60 min served as experimental parameters. For lubricated experiments, Aeroshell Grease 33 (Shell, Hamburg, Germany) was used as a lubricant, which has a base oil viscosity of 14.2 $mm^2/s$ and 3.4 $mm^2/s$ at 40 °C and 100 °C, respectively. This is a universally used grease for aerospace applications and contains corrosion/oxidation inhibitors along with extreme pressure additives in a lithium complex thickened synthetic base oil.

The topographical characteristics of the wear scar were analysed by secondary electron images of single beam SEM Philips XL 30S (Philips, Hamburg, Germany) and the wear volume was calculated with the help of a Sensofar Plµ Neox confocal microscope (Sensofar, Barcelona, Spain).

### 2.6. MD system setup

Equiaxed and acicular polycrystals with periodic boundaries in all directions were synthesised in DREAM.3D [27] with an identical average equivalent-sphere diameter of 16.5 nm. The generated voxelised microstructures were further processed via a custom script to obtain simulation domains of 60 × 60 × 30 $nm^3$. Atomic coordinates were populated on an α-Ti HCP lattice (a, c chosen consistent with the employed interatomic potential) and uniformly contracted by (empirically determined) 5 % prior to equilibration to compensate for the grain-boundary volume expansion introduced by the discrete voxel representation. For Ti-N systems, octahedral interstitial sites were partially occupied to achieve an overall composition of $TiN_{0.3}$ (one octahedral site per unit cell populated, yielding ~33 at.% N). The resulting pure-Ti systems contained ~6.0 × $10^6$ atoms, $TiN_{0.3}$ systems contained 8.5–8.8 × $10^6$ atoms. The MD models were developed to separately

study the influence of grain morphology and interstitial nitrogen on the mechanisms acting in the tribologically loaded Ti and $TiN_{0.3}$ systems.

All systems were energy-minimised and equilibrated in LAMMPS [28] at 300 K using periodic boundary conditions in x and y directions, and non-periodic and shrink-wrapped boundaries along z, until a stable volume and temperature were reached. The integration time step was 2 fs. Interatomic interactions were described by modified embedded atom method (MEAM) potentials: the Ti–Al parameterisation [29] (using Ti parameters only) for pure Ti, and a Ti–N parameterisation [30] for Ti–N systems. Ti–Ti interactions were identical across both parameter sets. To simulate the substrate, atoms in the bottom 3 Å along z were rigidly fixed, while a thermostat layer between 3 and 6 Å was coupled to a Langevin thermostat with a damping parameter of 0.5 ps. The remaining bulk region was thermostatted with a Langevin thermostat using a damping parameter of 6 ps to obtain realistic thermal conductivities.

Scratching was performed using a purely repulsive spherical implicit indenter with a force constant of 10 eV/Å$^3$, a radius of 30 nm, an indentation velocity of 5 m/s, and a scratching velocity of 20 m/s, due to MD timescale constraints. Forces on the indenter were recorded during the simulations. Each run was carried out for 6 ns, corresponding to a scratching distance of 120 nm (~two passes of the sample length). Fig. 2 represents the nanoscale scratching on polycrystalline $TiN_{0.3}$.

### 2.7. MD post-processing/evaluation

#### 2.7.1. Microstructure

The microstructure of the samples is visualized by performing polyhedral template matching (PTM) [31] on the geometry snapshots of the system. This allows a robust identification of the local lattice structure (HCP, FCC, BCC, "other") with little interference by temperature or local stresses. Useful atomic colouring schemes include one based on defects (different colours for the undisturbed lattice, grain boundaries/surfaces/point defects, stacking faults/twin boundaries) and another based on the lattice orientation (equivalent to electron backscatter diffraction imaging known from scanning electron microscopy). Note that for the $TiN_{0.3}$ samples, the N atoms at the octahedral positions were temporarily removed from the system before applying the PTM algorithm in order not to interfere with the local hcp lattice structure.

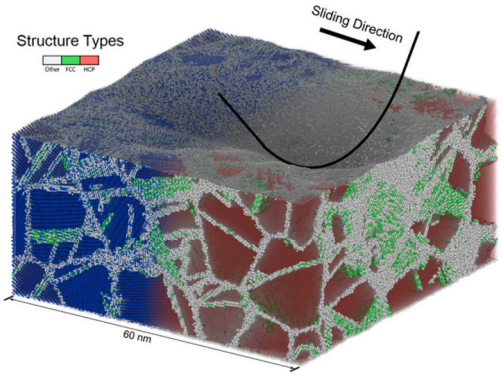


**Fig. 2.** Representative molecular dynamics simulation of nanoscale scratching on polycrystalline $TiN_{0.3}$. Introducing a degree of transparency to all HCP atoms (red) reveals the underlying grain structure, while regions of undefined (white) or FCC (green) coordination highlight deformation and defect formation beneath the indenter. Nitrogen atoms are shown in blue with a fading transparency gradient for improved visibility of the grain structure. In the simulation, nitrogen is uniformly distributed throughout all grains, although the experimental samples feature a slight gradient. This is justified by the entire MD system being a factor of 10 smaller in linear dimensions than a single experimental grain, as well as our main interest in differentiating between pure Ti and $TiN_{0.3}$. The spherical indenter's generatrix is rendered for visual reference. (For interpretation of the references to colour in this figure legend, the reader is referred to the web version of this article.)

#### 2.7.2. Contact forces

The forces acting on the indenter were obtained directly from the LAMMPS "fix indent" command, which outputs the three cartesian components of the indenter–substrate interaction force as a vector quantity.

#### 2.7.3. Contact area

To quantify the contact between the indenter and the substrate, the instantaneous contact area was estimated from the local atomic geometry. All substrate atoms within a specified cutoff distance from the indenter surface were identified as contact atoms. To determine an appropriate cutoff, the projected per-atom area was calibrated by dividing the known surface area of the undeformed substrate by the number of atoms contained in a surface slab of varying thickness corresponding to the cutoff distance. The resulting curve of projected per-atom area versus cutoff distance exhibits a plateau once additional atomic layers start being included. The beginning of this plateau marks the optimal cutoff, ensuring complete single-layer coverage without overestimating the contact area. The final contact area was obtained by multiplying this calibrated per-atom area with the number of atoms identified within the selected cutoff shell. To estimate the uncertainty in the calculated contact area, several cutoff values in the vicinity of the identified optimum were evaluated, allowing the determination of error bars. After selecting the atoms in contact with the indenter, spatial binning was applied to project their positions onto the relevant reference planes. Projection onto the plane parallel to the surface (z-axis = surface normal) yielded the normal (normal-force-resisting) contact area, while projection onto the yz-plane (normal to the scratching direction) provided the plowing (tangential) contact area. These projections thus quantify the respective areas over which normal and tangential forces act during the scratching process.

#### 2.7.4. Scratch profiles

To compare surface deformation between systems, the scratch profiles were analysed. Due to the periodic boundary conditions, the indenter traversed the simulation domain twice, passing through its own initial trail. To obtain statistically robust results with associated uncertainties, the surface height profile was averaged over the region where a fully developed scratch was present. Since the indenter remained in contact with the surface after initial penetration, its direct influence on the topography was excluded to avoid artificial distortion of the scratch shape. This was achieved by evaluating the surface height line along the indenter's central trajectory and omitting regions corresponding to the virgin (unindented) surface and the indenter's current position. The resulting height profiles were then averaged along the scratching direction to yield a mean scratch cross-section with standard deviation. This approach also enables visualisation of the scratch evolution over time once sufficient scratching distance has been covered to obtain a stable profile.

## 3. Results and discussions

### 3.1. XRD analysis

The XRD patterns for all the laser-modified samples are shown in Fig. 3. The untreated sample exhibited only α-Ti peaks in the (1 0 0), (0 0 2), and (1 0 1) directions. Similarly, the Ti Ar/Ar (melted and smoothened in argon) and Ti Air/Ar (melted in air and smoothened in argon) samples also showed α-Ti peaks and no peaks of the stoichiometric or non-stoichiometric form of $TiO_2$ were detected in the Ti Air/Ar sample. However, in the untreated α-Ti sample, the strong significant peak of α-Ti (0 0 2) vanished at other ψ angles, indicating the presence of strong textures in the untreated or raw sample due to the manufacturing process. In the case of the Ti $N_2$/Ar (melted in nitrogen and smoothened in argon) sample, no TiN peaks were observed. However, some weak signals corresponding to non-stoichiometric TiN,

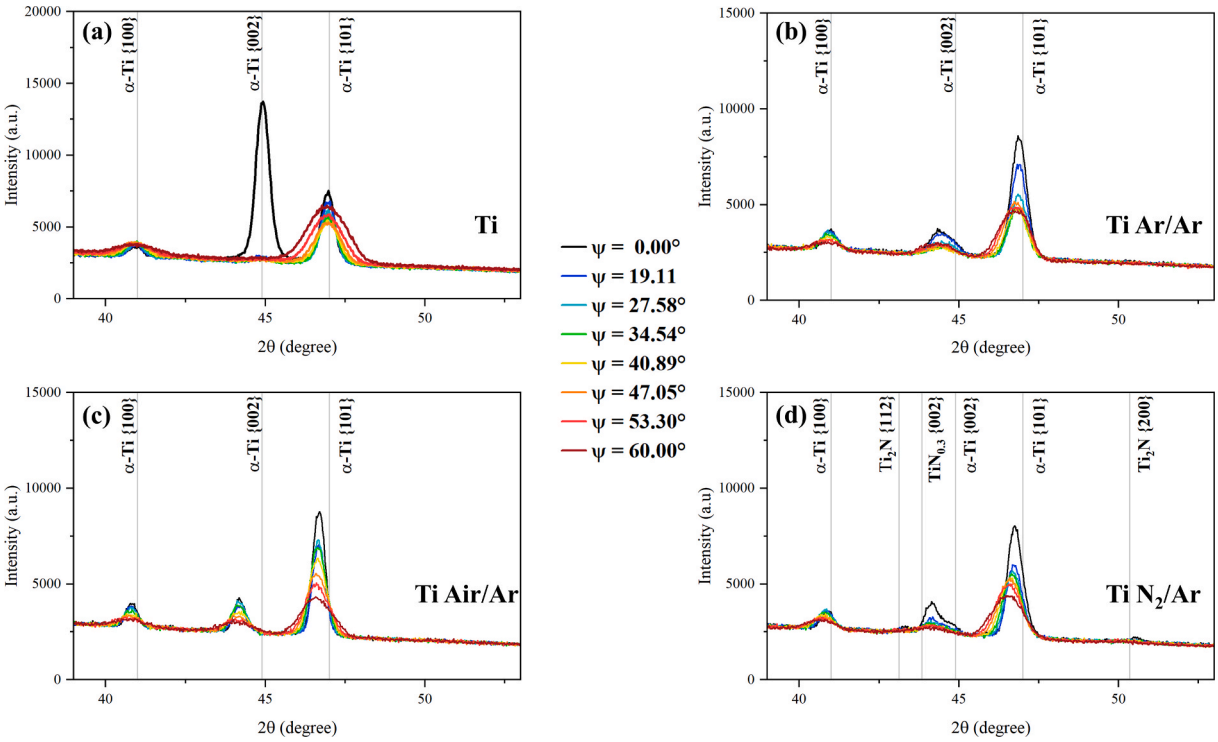


**Fig. 3.** XRD of (a) Ti, (b) Ti Ar/Ar, (c) Ti Air/Ar, (d) Ti $N_2$/Ar.

primarily $TiN_{0.3}$ and $TiN_{0.5}$, were identified alongside α-Ti peaks.

Apart from the untreated sample, all the peaks in other samples exhibited a red shift, likely due to lattice distortion. The c/a ratio of the untreated sample was found to be 1.585, and it was 1.605, 1.609, and 1.600 for Ti Air/Ar, Ti $N_2$/Ar, and Ti Ar/Ar, respectively. For the samples lasered in nitrogen and air atmosphere, the increase in c/a ratio could be the result of nitrogen and oxygen occupying the interstitial positions in the Ti lattice [8]. The octahedral vacancy of α-Ti has a radius of 0.61 Å, which is similar to the neutral atomic radii of N (0.71 Å) and O (0.66 Å) atoms. However, an increase in the c/a ratio was also observed for the Ti Ar/Ar samples lasered in an argon atmosphere. Argon, being an inert gas, does not react with Ti during laser surface modification and, therefore, does not occupy any interstitial positions in the Ti lattice. Therefore, the increase in the c/a ratio can be attributed to the difference in the coefficient of thermal expansion along the c and a axes in the Ti lattice. The α-Ti has hexagonal closed pack (HCP) lattice structure, which has different packing densities along the c axis and hence the coefficient of thermal expansion is different along the c and a axes. This leads to anisotropic lattice expansion [8] and contraction during the laser modification, resulting in lattice distortion.

### 3.2. Microstructural characterization

Fig. 4 shows the FIB cross-sections of Ti Ar/Ar, Ti $N_2$/Ar, and Ti Air/Ar samples. All three samples reveal different microstructures. The Ti Ar/Ar samples exhibit only very fine criss-cross acicular grains with a length between 0.4 and 1 μm, and a width between 0.08 and 0.14 μm (Fig. 4(a)). These criss-cross acicular grains are often termed as α laths or α′-Ti [32]. During the laser surface modification, the α-Ti undergoes α/β transformation at a temperature of ~900 °C. The high-temperature stable body-centred cubic (BCC) β phase cools down to the low-temperature stable HCP α phase. The temperature gradient for laser melting and solidification is relatively high (~3000 °C/s), which leads to a diffusion-less shear-type transition, and the β phase transforms into martensitic α′-Ti [32]. The Ti $N_2$/Ar samples have large equiaxed grains with varying diameters between 0.2 and 0.8 μm, and fine acicular grains with lengths and widths ranging from 1 to 1.8 μm and 0.1 to 0.15 μm, respectively (Fig. 4(b)). Finally, the Ti Air/Ar samples also show criss-cross acicular grains like the Ti Ar/Ar samples, but with coarser grains (lengths ranging from 1 to 6 μm and widths ranging from 0.15 to 0.35 μm) (Fig. 4(c)).

Laser processing of Ti in nitrogen atmosphere produces a dual-phase microstructure comprising equiaxed and acicular grains, governed by nitrogen absorption dynamics and rapid thermal cycles. Nitrogen molecules get adsorbed on the surface of Ti under laser heating via a charge transfer mechanism [33]. The adsorbed nitrogen then dissociates into atomic nitrogen due to laser induced thermal energy, which in turn leads to diffusion of atomic nitrogen into the Ti lattice occupying the octahedral interstitial sites and forming $TiN_{0.3}$ and $Ti_2N$ (also known as α-Ti (N) solid solutions) [34]. The high cooling rates in the laser treatment process tend to suppress the growth of acicular α′-Ti in a nitrogen-rich atmosphere. It reduces the time for diffusion-controlled β → α phase transformation, favouring the nucleation of equiaxed α-Ti(N) grains over the acicular structure [35]. Previous studies have reported that for α-Ti substrate lasered in nitrogen atmosphere, the equiaxed α-Ti(N) contains a higher nitrogen content of (0.3–15 wt%), whereas the acicular grains have a lower nitrogen content of (0.1–0.3 wt%) [33,36]. The large nitrogen atom (0.71 Å) leads to high lattice strains inside the α-Ti lattice, which pin dislocations and hinder dislocation glide. Dislocation glide is important for martensitic shear, which is important for the β → α′ phase transformation, leading to the formation of acicular grains. Fig. 4(b) also shows that acicular grains dominate at higher depths, and equiaxed grains dominate near the surface of Ti. This gradient aligns with nitrogen's diffusion-limited penetration, where near-surface regions exhibit more equiaxed α-Ti(N) due to abundant nitrogen, transitioning to acicular martensite in the nitrogen-depleted core. Fig. 5 shows the bright field and high annular angular diffraction (HAADF) STEM images of the Ti $N_2$/Ar substrate. In the bright field images, the equiaxed grains exhibit uniform contrast, consistent with homogeneous α-Ti(N) solid solution formation. Conversely, acicular grains show variation in the internal contrast, suggesting substructural heterogeneity. The darker regions in the HAADF image indicate higher nitrogen

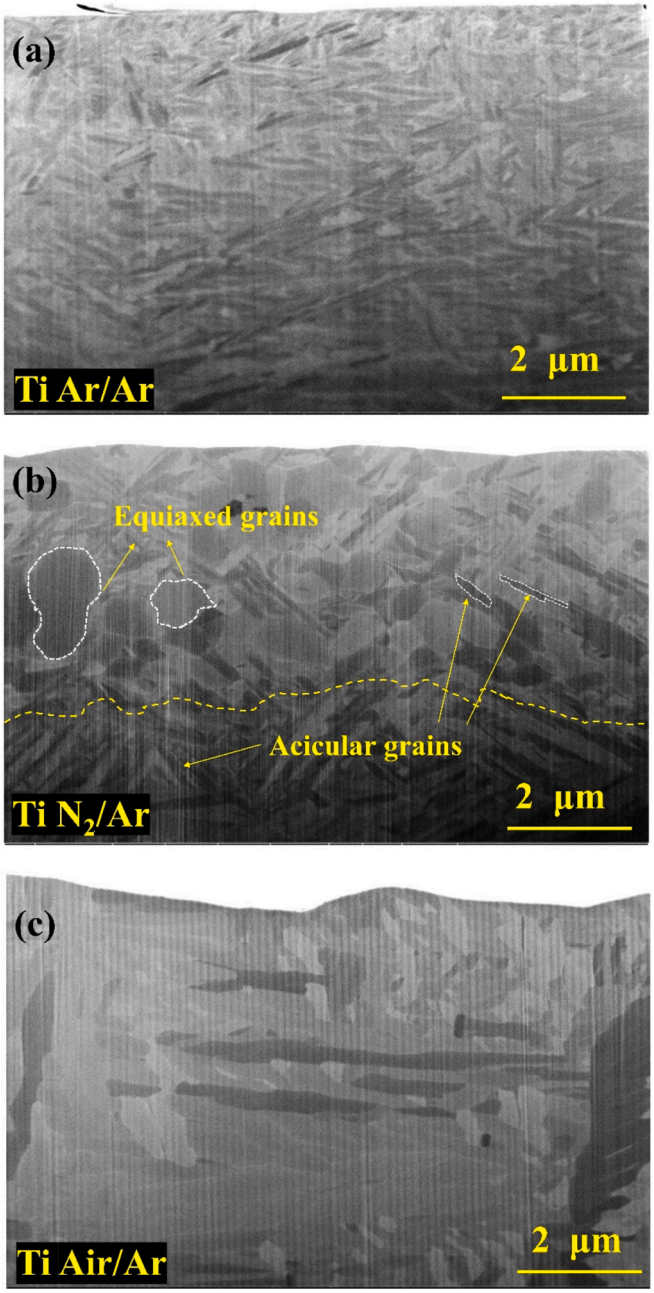


**Fig. 4.** FIB cross-sections of (a) Ti Ar/Ar, (b) Ti $N_2$/Ar, and (c) Ti Air/Ar.

content due to a reduced average atomic number (Z-contrast). The predominantly dark equiaxed grains can be another indication of a greater nitrogen concentration, while the brighter zones within the acicular grains may be due to a lower interstitial nitrogen concentration.

Similar to nitrogen, oxygen also occupies the vacant octahedral sites in the α-Ti lattice, but its diffusion behaviour differs significantly. Oxygen exhibits significantly lower activation energy for diffusion than nitrogen (~156 kJ/mol for oxygen vs. ~486 kJ/mol for nitrogen), and threefold higher solubility [37,38]. Therefore, when the Ti sample is lasered in air, oxygen preferentially adsorbs and incorporates into the Ti lattice due to higher chemical affinity. This is also in line with the previous work done by our group [12]. During β → α phase transformation in the presence of oxygen, oxygen stabilises the α/α′ phases but, unlike nitrogen, does not suppress the formation of martensitic laths (acicular grains). This occurs because oxygen's smaller atomic radius (0.66 Å) compared to that of nitrogen (0.71 Å) induces less lattice distortion, allowing dislocations to propagate and nucleate acicular α′ grains [39]. Therefore, only crisscross acicular grains were observed in case of Ti lasered in air (Fig. 4(c)).

The shape of the grains in the microstructure of Ti treated under the different gaseous atmospheres discussed in the paragraphs above complies well with the literature available till date [32,33,36,39]. However, the grain size obtained in the present investigation after the smoothening step was quite different from the sizes reported in the literature. To investigate this, FIB cross-sections were cut out from the first laser treatment step, i.e., melting in the presence of argon (Ti Ar), nitrogen (Ti $N_2$), and air (Ti Air). The microstructures for both the laser treatment step (melting and smoothening) were compared to analyse the reason behind the difference in the grain sizes.

Fig. 6. shows the FIB cross-sections of Ti Ar (after the melting step) and Ti Ar/Ar (after the smoothening step). We observed that after the first laser step, there were some voids in the microstructure, which were eliminated after the second laser step. Balla et. al. [25] also reported that the second laser step helps eliminating voids that occur after the first laser step. The depth of the laser-affected zone after the first laser step was found to be ~4 µm, which increases to ~10 µm after the second laser step. The repeated laser treatment in argon increases the melt pool depth due to residual heat retention in the pre-modified layer [40]. As shown in Fig. 6(a), the first laser treatment results to the formation of α′-Ti martensite due to rapid solidification during the laser process. This refined microstructure lowers the thermal conductivity, acting as a "heat trap" and promoting a deeper laser affected zone in the subsequent passes. However, there was no considerable change in the grain size after the first and the second laser step.

The formation of precipitates of nitrides and oxides during the laser surface treatment of α-Ti has been well reported in the literature [41,42]. Fig. 7 shows that for the samples lasered in nitrogen and air, the size of the grains increases in both cases after the second smoothening step in the presence of argon. However, we see a larger increase in size of the acicular grains for the Ti lasered in air than for the one lasered in

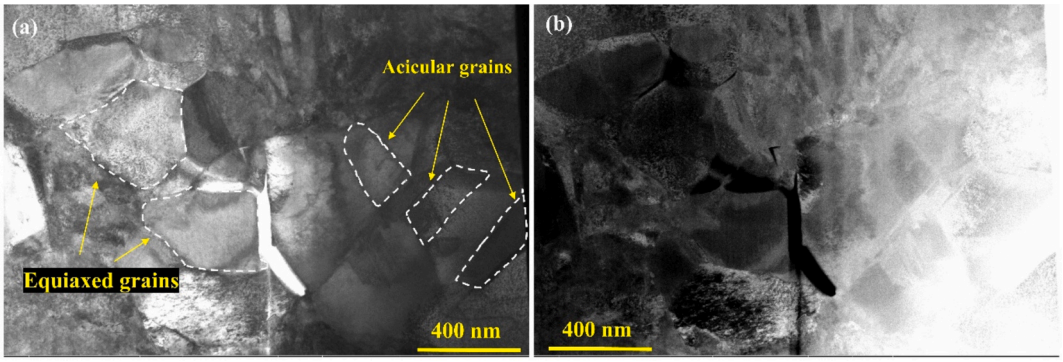


**Fig. 5.** STEM image of lamella prepared from Ti $N_2$/Ar substrate (a) bright field and (b) HAADF.

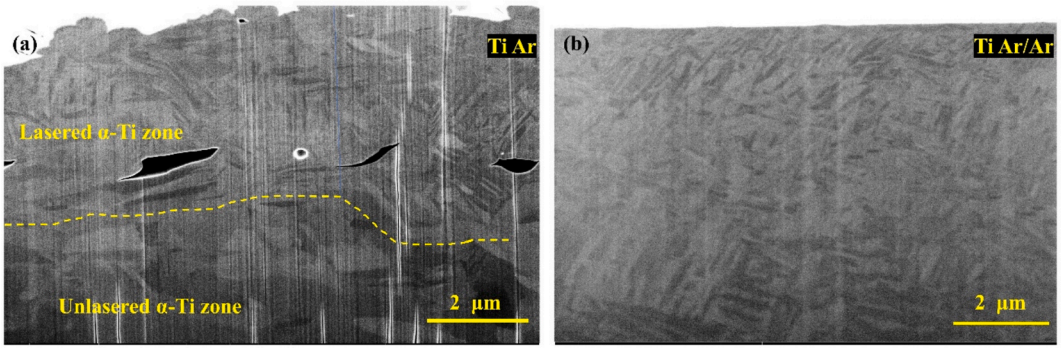


**Fig. 6.** FIB cross-section of (a)Ti Ar and (b) Ti Ar/Ar.

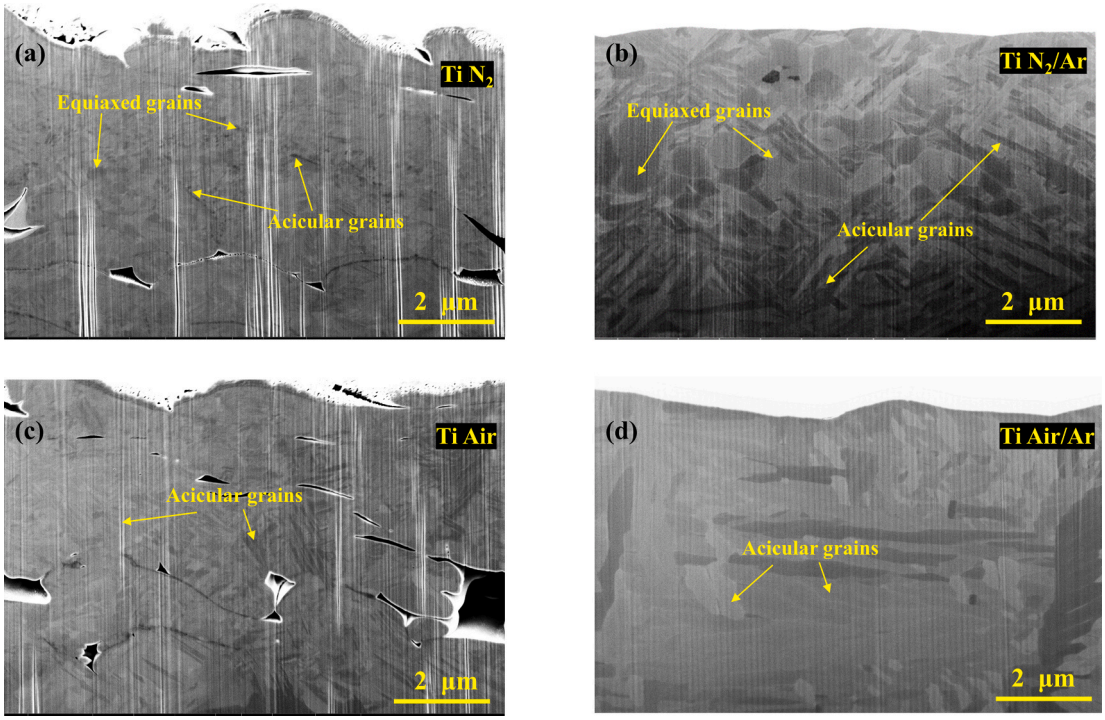


**Fig. 7.** FIB cross-section of (a) Ti $N_2$, (b) Ti $N_2$/Ar, (c) Ti Air, and (d) Ti Air/Ar.

nitrogen. During the first laser step (melting in reactive atmosphere), the reactive gas (nitrogen and oxygen (for air)) is in abundance and rapidly dissolves into the molten Ti. This creates supersaturated conditions even at the high cooling rates of the laser treatment process and leads to the formation of precipitates of $TiN_x$ and $TiO_x$. These precipitates act as pinning points for grain growth, suppressing grain boundary migration and leading to the formation of very fine grains (Fig. 7(a) and (c)) through Zener pinning. During the second laser step (smoothening in argon atmosphere), argon provides no source of nitrogen or oxygen and limits supersaturation. The precipitates formed after the first laser step either dissolve into the liquid phase and form a solid solution with the Ti (occupying interstitial positions), or the precipitates agglomerate to form coarser particles through Ostwald ripening. Both cases result in loss of Zener pinning and lead to an increase in grain size during the second laser step. However, the observed differences in grain sizes after the second laser treatment, specifically for Ti samples initially irradiated in nitrogen and air, can be attributed to the formation of small amounts of $TiN_{0.3}$ and $Ti_2N$, as confirmed by XRD analysis (see Fig. 3(d)) for the Ti $N_2$/Ar sample. Notably, TiN possesses a high melting point of approximately 3000 °C, which is comparable to the temperatures reached during laser surface treatment. Therefore, it is possible that these refractory nitride phases are left behind in the form of precipitates (although little in amount) and act as a pinning site, but with very low efficacy of Zener pinning. For the Ti irradiated in the presence of oxygen, no XRD peaks of $TiO_x$ were observed after the second laser treatment of the Ti Air/Ar (Fig. 3(c)). Therefore, the grain growth is larger after the second laser step because of the absence of Zener pinning.

### 3.3. *Mechanical properties*

The box plots of hardness and elastic modulus values for various samples are shown in Fig. 8. The hardness values for Ti Ar/Ar were higher than those of Ti, which can be attributed to grain refinement after the two-step laser process. It can also be seen in Fig. 6(a), where the laser-affected zone has a fine martensitic acicular microstructure, whereas the raw Ti surface beneath it has a fairly large equiaxed microstructure. The hardness values for Ti Air/Ar and Ti $N_2$/Ar were twice as high as those of Ti. The interstitial nitrogen and oxygen significantly enhance the hardness of Ti through solid solution strengthening [8,11,12,18,43]. It can be observed that nitrogen and oxygen had a similar effect on increasing the hardness values of Ti; however, the dissolution of nitrogen would have been less in the Ti

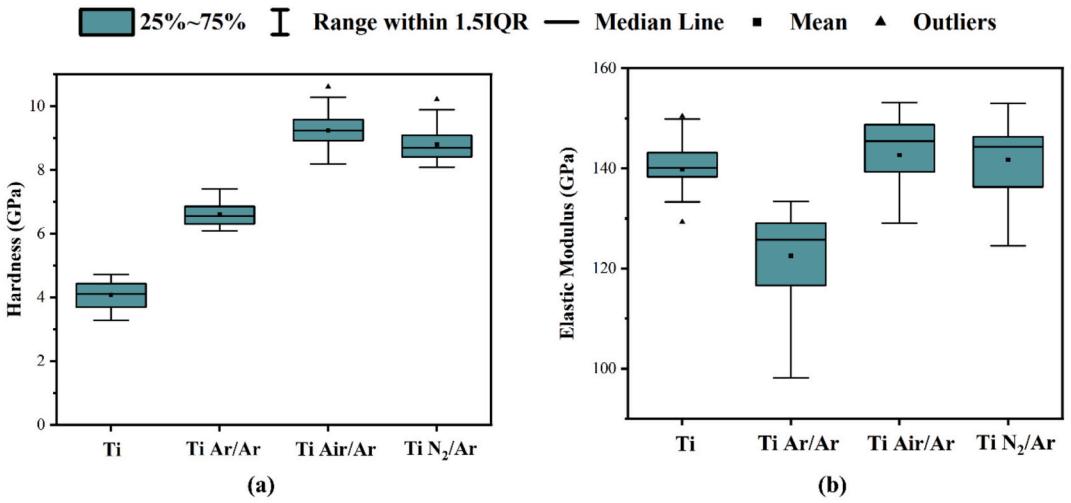


**Fig. 8.** Box plot of (a) hardness and (b) elastic modulus for values for laser treated and untreated Ti. The whiskers represent the range between 1.5 times the interquartile range (IQR).

matrix because of its lower solubility than oxygen. These results are also corroborated by the findings of Frederik et. al. [8]. However, the elastic modulus exhibits a unique behaviour across different samples. The elastic modulus of Ti, Ti Air/Ar, and Ti $N_2$/Ar were almost the same. By contrast, the elastic modulus of Ti Ar/Ar not only exhibited lower values but also showed greater variability across different indentations. This reduction and increased scatter in elastic modulus can be attributed to anisotropic lattice expansion induced by the laser treatment, which promotes texture formation within the Ti lattice. Since the elastic modulus is orientation-dependent, this enhanced texture leads to significant variation in the measured values for Ti Ar/Ar.

For Ti Air/Ar and Ti $N_2$/Ar, however, the elastic modulus returns to values characteristic of untreated Ti. This is because the presence of interstitials such as oxygen and nitrogen induces a more symmetric lattice strain, effectively suppressing the development of textures. [44].

### 3.4. Tribological behaviour

The variation of the coefficient of friction over the sliding distance of various laser-treated and untreated samples lubricated with Aeroshell grease is shown in Fig. 9(a). Ti showed high fluctuations in the coefficient of friction during the initial running-in stage and then achieved a steady-state coefficient of friction between 0.18–0.19. Ti Air/Ar and Ti $N_2$/Ar exhibited a constant coefficient of friction from the onset of sliding (i.e., no running-in) and had a steady-state coefficient of friction between 0.16–0.17. Contrastingly, Ti Ar/Ar showed dual behaviour. For some tests, Ti Ar/Ar (denoted as Ti Ar/Ar (W)) behaved similarly to Ti, i.e., high fluctuations in the coefficient of friction during the running-in stage and then achieving a steady state coefficient of friction of 0.16. In other tests, Ti Ar/Ar (denoted as Ti Ar/Ar (N)) behaved like Ti Air/Ar and Ti $N_2$/Ar, where it had a consistent steady-state of coefficient of friction between 0.18 and 0.19.

Analogous behaviour was also seen with wear volume measurements. Ti showed the highest wear, and for Ti Air/Ar and Ti $N_2$/Ar, the wear volume could not be quantified as the roughness of the scar was similar to the roughness of the original surface, indicating minimal wear. The Ti Ar/Ar sample repeated the same behaviour that it showed for the results of the coefficient of friction. Some samples of Ti Ar/Ar behaved like untreated Ti, with high wear volumes, and some like Ti Air/Ar and Ti $N_2$/Ar, with minimal wear. Consequently, the error bar shown in Fig. 9(b) for Ti Ar/Ar is also large by comparison.

The high chemical reactivity of Ti leads to strong adhesive bonds

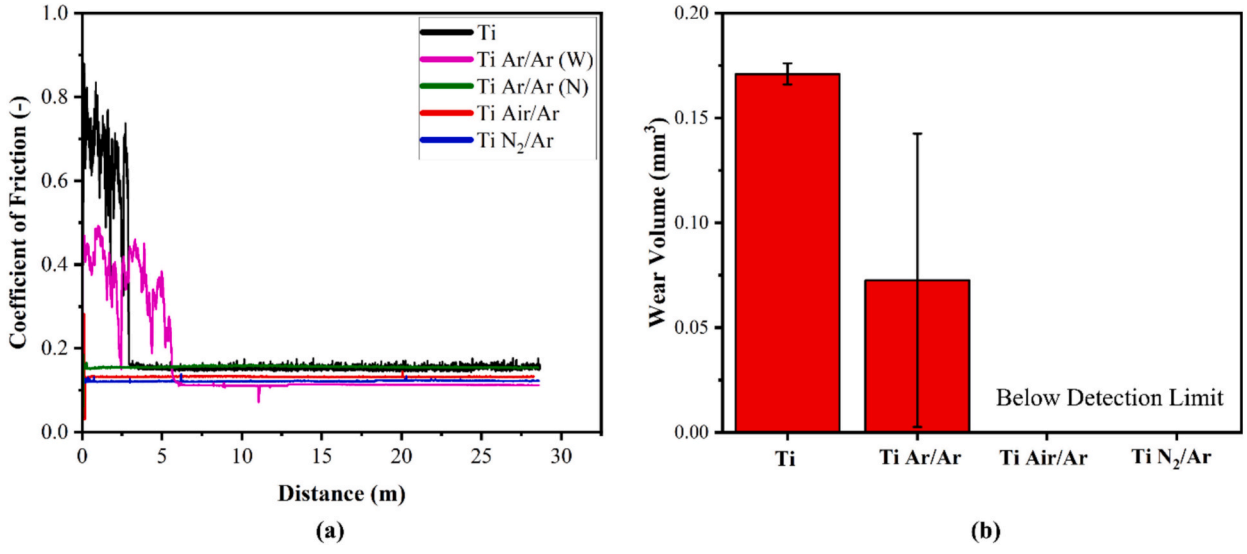


**Fig. 9.** (a) Coefficient of friction and (b) wear volume data of laser treated and untreated Ti under grease lubrication.

with the countersurface. Titanium has non-localised valence electrons that readily form bonds with other materials (e.g. iron in steel). This results in adherence of Ti to the counter body, forming junctions that fracture during the sliding, and pulling out material from the Ti surface [11,12,18]. Also, a low hardness of 4 GPa and limited work hardenability further exacerbate wear. Fig. 10(a) shows the SEM image of the wear scar of untreated Ti and signs of adhesive material removal can be observed in the direction of sliding.

Ti Air/Ar and Ti $N_2$/Ar exhibited negligible measurable wear, with only minor surface smoothening observed, indicative of micro-plastic deformation rather than material removal. (Fig. 10(d) and (e)). The roughness of the wear scar was the same as the roughness of the original substrate, and therefore, the wear volume could not be quantified. For Ti Air/Ar and Ti $N_2$/Ar, oxygen and nitrogen occupy the interstitial positions inside the Ti lattice (Section 3.2). The oxygen and nitrogen atoms change the electron density around the Ti atom. This saturates the Ti's valence bonds, localises the electrons and reduces the surface reactivity. The electronic passivation created by oxygen and nitrogen occupying the interstitial positions inside the Ti lattice lowers the adhesive tendency, preventing material transfer and cold welding. From Fig. 8, it is evident that the interstitial oxygen and nitrogen influence the hardness (H) and elastic modulus (E) of the laser-treated Ti surface. This change results in a change in H/E (resistance to elastic deformation) and $H^3/E^2$ (resistance to plastic deformation) values for the laser-treated Ti surface. The high H/E and $H^3/E^2$ values for Ti Air/Ar and Ti $N_2$/Ar (Fig. 11) are also in agreement with the wear observed on the surface. The addition of oxygen and nitrogen in the interstitial positions of the Ti lattice tends to shift the failure mode in the material from ductile to brittle [6,11,18]. Hence, the multi-faceted wear mechanism shifts from adhesion to mild abrasion.

The inconsistent tribological behaviour of the Ti Ar/Ar laser treated samples, oscillating between Ti–Ti Air/Ar and Ti $N_2$/Ar responses, can be attributed to heterogeneous oxygen adsorption despite of argon purging. As stated earlier in the manuscript, Ti has a very high affinity for oxygen, and adhesive wear mechanisms primarily govern the wear in Ti. It is safe to assume that some oxygen-rich zones could have been formed on the surface even after argon purging. Although the three different microstructures (Fig. 4) obtained for the laser-treated Ti in different ambient environments suggested that there are different mechanisms at play for grain formation, which is mainly because of the oxygen and nitrogen atoms occupying interstitial positions inside the Ti lattice. However, the tribological results for Ti Ar/Ar showed a completely different story. The tribological results can easily be affected by the presence of oxygen on the surface. It is believed that the places where a localised oxygen-rich zone is present on the surface of Ti Ar/Ar, it reduces running-in, making Ti Ar/Ar behave like Ti Air/Ar and Ti $N_2$/Ar. Since this oxygen contamination is just localised on the surface, it does not show any subsurface effect as was seen for Ti Air/Ar and Ti $N_2$/Ar. Also, the Ti Ar/Ar samples have smaller grains, which increases surface reactivity and promotes trapping of oxygen on the surface. This trapped oxygen can reduce adhesion, which may explain why Ti Ar/Ar shows inconsistent wear behaviour. Areas without oxygen

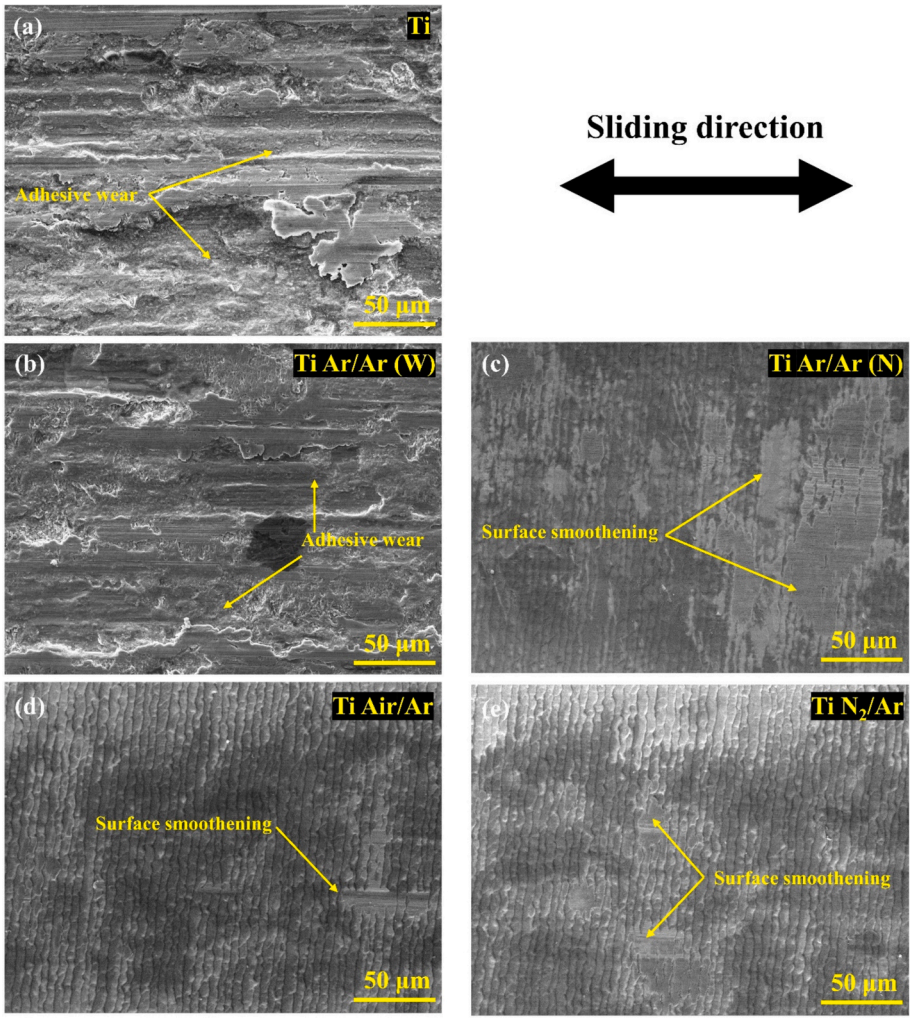


**Fig. 10.** SEM images of wear scar of (a) untreated Ti, (b) Ti Ar/Ar (W), (c) Ti Ar/Ar (N), (d) Ti Air/Ar, and (e) Ti $N_2$/Ar.

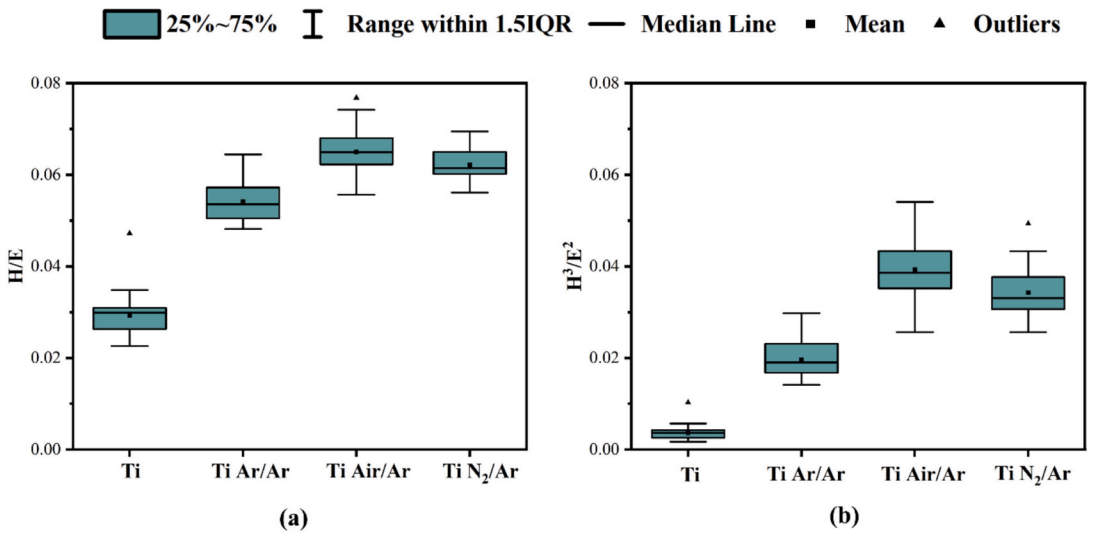


**Fig. 11.** Box plot of (a) H/E and (b) $H^3/E^2$.

contamination experience severe adhesive wear. Wear measurements show that when adhesive wear is absent, Ti Ar/Ar (labeled Ti Ar/Ar (N)) has almost no wear in a lubricated environment, meaning no significant plastic deformation. In this case, the wear can be correlated to the resistance to elastic deformation, H/E, which is almost the same for Ti Ar/Ar, Ti Air/Ar, and Ti $N_2$/Ar (Fig. 11(a)). Whereas, when the Ti Ar/Ar (Ti Ar/Ar (W)) behaved like untreated Ti, the wear mechanisms can be correlated to the resistance to plastic deformation, $H^3/E^2$, and here we see a clear difference in the values from Ti Air/Ar and Ti $N_2$/Ar (Fig. 11 (b)). The wear volume obtained for Ti Ar/Ar (W) in this case is more than what obtained in Ti Air/Ar and Ti $N_2$/Ar, as the $H^3/E^2$ value is lower for Ti Ar/Ar, and the wear volume is lower than that of Ti as the $H^3/E^2$ of Ti Ar/Ar are higher than Ti. To investigate the oxygen and nitrogen on the surface and in the interstitials, XPS studies were also carried out, but nothing substantial came out from it because of the low oxygen and nitrogen concentration (<detection limit), and therefore, are not reported in the present manuscript.

After analysing the wear behaviour, the steady state coefficient of friction shown in Fig. 9(a) can be attributed to the boundary lubrication of grease. After initial surface interaction (running-in), the coefficient of friction is controlled by grease rheology and not by substrate properties. The presence of interstitial oxygen and nitrogen in the near-surface region (introduced via laser processing in air and nitrogen) is crucial. These interstitials saturate titanium's valence bonds, reduce chemical reactivity, and suppress adhesive wear, allowing the friction to stabilise quickly, which can be viewed by the negligible running-in in Fig. 9(a). Surfaces lacking sufficient interstitials behave similarly to untreated Ti, with high initial friction and adhesive wear. Moreover, the increased hardness from interstitial solid solution strengthening limits plastic deformation and junction growth, further reducing adhesive tendencies and stabilising friction. Once adhesive wear is suppressed (either after running-in or immediately on surfaces with interstitials), boundary lubrication by the applied grease (AeroShell) dominates, resulting in a steady-state coefficient of friction that is nearly identical for all surface conditions. It was also demonstrated in our previous study, where additional experiments with additive-free oils confirmed that the steady-state coefficient of friction is governed by the lubricant, rather than the specific surface treatment [12,18].

### 3.5. MD simulation study

The scratch profiles reveal distinct deformation behaviours between Ti and $TiN_{0.3}$ systems. Pure Ti exhibits a pronounced ridge build-up along the scratch edges, while $TiN_{0.3}$ systems show little to no such accumulation. In the acicular $TiN_{0.3}$ microstructure, regions adjacent to the indenter even lie slightly below the original surface, suggesting that deformation occurs through grain-scale displacement rather than localised material pile-up. Overall, $TiN_{0.3}$ systems undergo stronger plastic deformation, with scratch depths approximately 5–8 Å greater than those in Ti (Fig. 12). These trends are consistent with the recorded force evolution. In Ti systems, the tangential (Fx) and normal (Fz) forces are of similar magnitude and evolve smoothly as the indenter progresses, reflecting continuous material flow in front of the indenter. In contrast, $TiN_{0.3}$ systems display markedly different force characteristics. For the equiaxed $TiN_{0.3}$ microstructure, both Fx and Fz are 50–80 % higher than in pure Ti, whereas the acicular $TiN_{0.3}$ system exhibits a lower tangential force and comparable normal force. The fluctuations observed in the $TiN_{0.3}$ force curves indicate a stronger sensitivity to the local grain structure and heterogeneous deformation response.

Consistently, the equiaxed systems required higher initial tangential and normal forces to reach the target indentation depth. These observations are further supported by the projected contact area evolution. Throughout the simulations, $TiN_{0.3}$ systems exhibited 40–50 % smaller contact areas in both projection planes (corresponding to the regions counteracting the tangential and normal forces), whereas the equiaxed

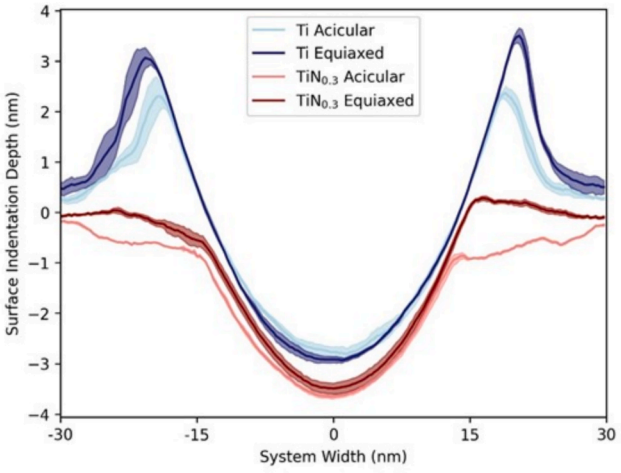


**Fig. 12.** Median depth profiles of the MD-simulated scratch experiments on equiaxed and acicular microstructures of Ti and $TiN_{0.3}$. The error ranges reflect temporal topographic variations within regions featuring equilibrated scratch profiles. Note the periodic boundary conditions along the horizontal dimension.

systems maintained larger contact areas over the entire scratching trajectory (Fig. 13). The plots correlating the tangential and normal forces with their corresponding projected contact areas (panels e and f) indicate strain hardening as smaller resisting contact areas require equal forces. The equiaxed systems require higher initial forces to reach the target indentation depth and maintain larger contact areas throughout the simulation. Conversely, the $TiN_{0.3}$ systems exhibit smaller contact areas, indicative of higher stiffness and hardness at the grain level.

These results indicate that while the $TiN_{0.3}$ grains exhibit higher grain-level stiffness and hardness (reflected by the larger required forces and smaller effective contact areas), the overall deformation behaviour of the polycrystalline $TiN_{0.3}$ systems is governed by the grain boundary network. The unsteady force response and localised subsurface displacement suggest that plastic accommodation occurs preferentially

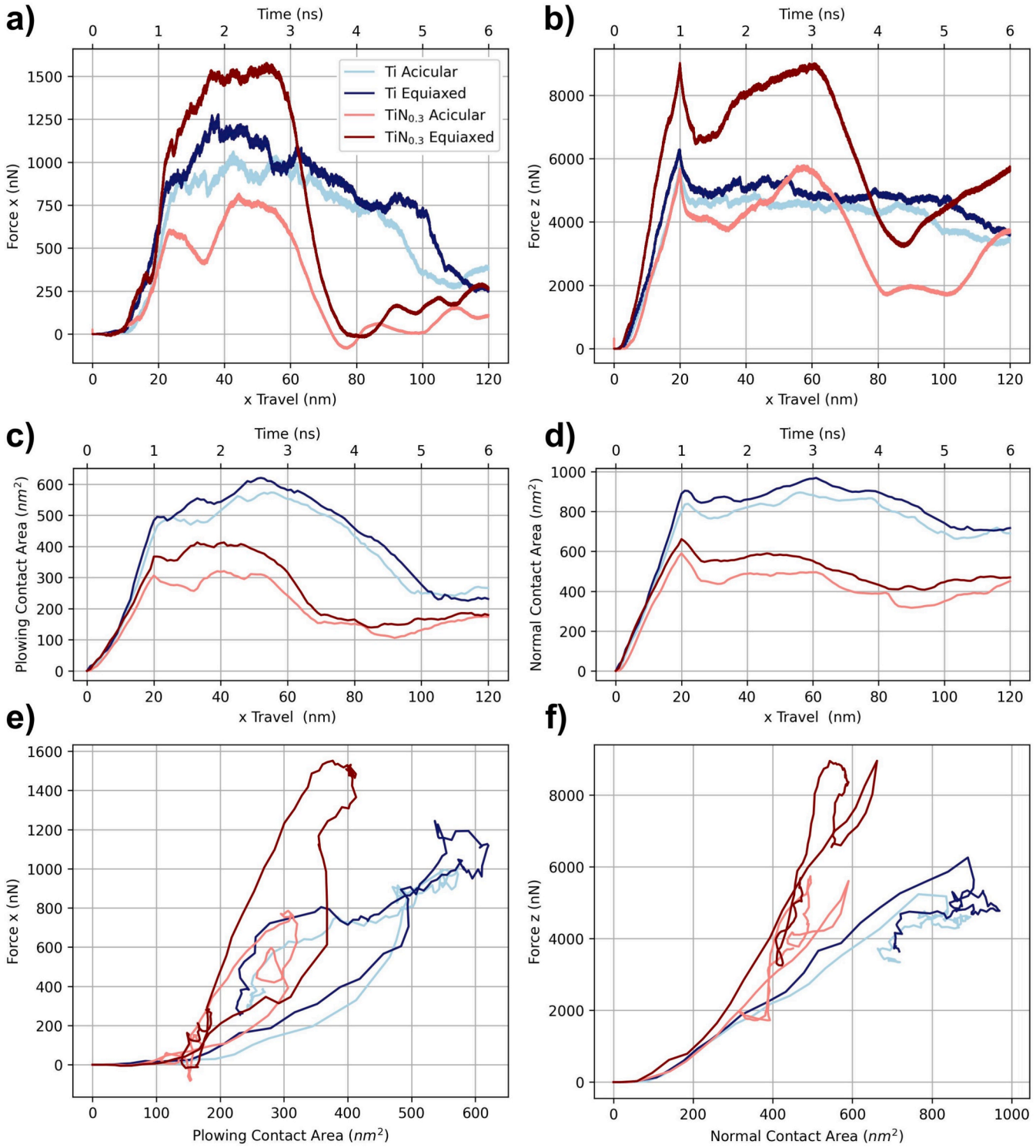


**Fig. 13.** Analysis of MD-simulated indenter counterforces and contact areas for Ti and $TiN_{0.3}$ systems with acicular and equiaxed microstructures. (a and b) Tangential (Force x) and normal (Force z) forces as a function of indenter travel distance. (c and d) Evolution of the projected plowing and normal contact areas during the scratch. (e and f) Correlation plots of tangential and normal forces versus their corresponding projected contact areas.

along grain boundaries rather than through intragranular plasticity, resulting in a more heterogeneous deformation mode. The acicular $TiN_{0.3}$ system required lower forces to reach the same indentation depth, which may be attributed to the preferred orientation of some elongated grains that facilitate grain boundary-mediated deformation. It should also be noted that the initial acicular $TiN_{0.3}$ microstructure contained small voids arising from incomplete folding of grains across periodic boundaries, which may have further contributed to the reduced load response. Similar voids are also visible in the STEM images (Fig. 5) of the Ti $N_2$/Ar sample.

Adding nitrogen into the interstitial sites of titanium introduces local lattice strain and distortion. During deformation, these distortions affect the positions of the surrounding titanium atoms, which are used as a reference for structural identification with the PTM method. Since PTM relies on the accurate detection of ideal local atomic environments and does not account for interstitial atoms, the presence of nitrogen reduces the degree of local order that can be recognised as a perfect lattice. Consequently, $TiN_{0.3}$ systems are more challenging to analyse in terms of microstructural evolution using PTM-based approaches (Fig. 14).

Together, the MD simulations show that the enhanced hardness of the $TiN_{0.3}$ microstructures originates at the grain scale, whereas the overall material response is governed by how deformation is accommodated along the grain boundary network. By linking the experimentally observed scratch behaviour to the underlying deformation mechanisms, the MD simulations provide the mechanistic context necessary to interpret the contrasting tribological responses of Ti and $TiN_{0.3}$. For detailed views of prevailing mechanisms, the reader is referred to the supplementary material.

## 4. Conclusion

This study demonstrates that the nature of the gaseous environment during laser surface treatment critically influences the microstructure, mechanical properties, and tribological behaviour of commercially pure α-Ti. Laser melting in air introduces interstitial oxygen that preferentially incorporates into the titanium lattice due to its higher chemical affinity and lower diffusion activation energy compared to nitrogen. This results in the formation of acicular martensitic grains with increased grain size after surface smoothening, fostering solid solution strengthening and passivation of titanium's valence bonds. Consequently, Ti Air/Ar samples show enhanced hardness, stable friction, and minimal adhesive wear attributed to electronic passivation lowering surface reactivity.

Nitrogen-rich laser atmospheres create a dual-phase microstructure comprising both equiaxed and acicular grains. Although nitrogen diffuses more slowly and has lower solubility, it forms TiN solid solutions that induce lattice strain, pinning dislocations and impeding plastic deformation. Ti $N_2$/Ar samples exhibit similar hardness and friction improvements to those treated in air, but with increased heterogeneity due to varying nitrogen concentrations within the grains. Ti $N_2$/Ar samples contributed to enhanced wear resistance by shifting failure modes from ductile adhesion to mild abrasion.

The origins of the higher resistance to deformation and wear lies in $TiN_{0.3}$ promoting grain boundary-mediated plastic accommodation and reducing material pile-up relative to pure Ti, as unveiled using molecular dynamics simulations of nanoscale scratching on polycrystalline $TiN_{0.3}$ and Ti systems. Incorporation of nitrogen in interstitial sites

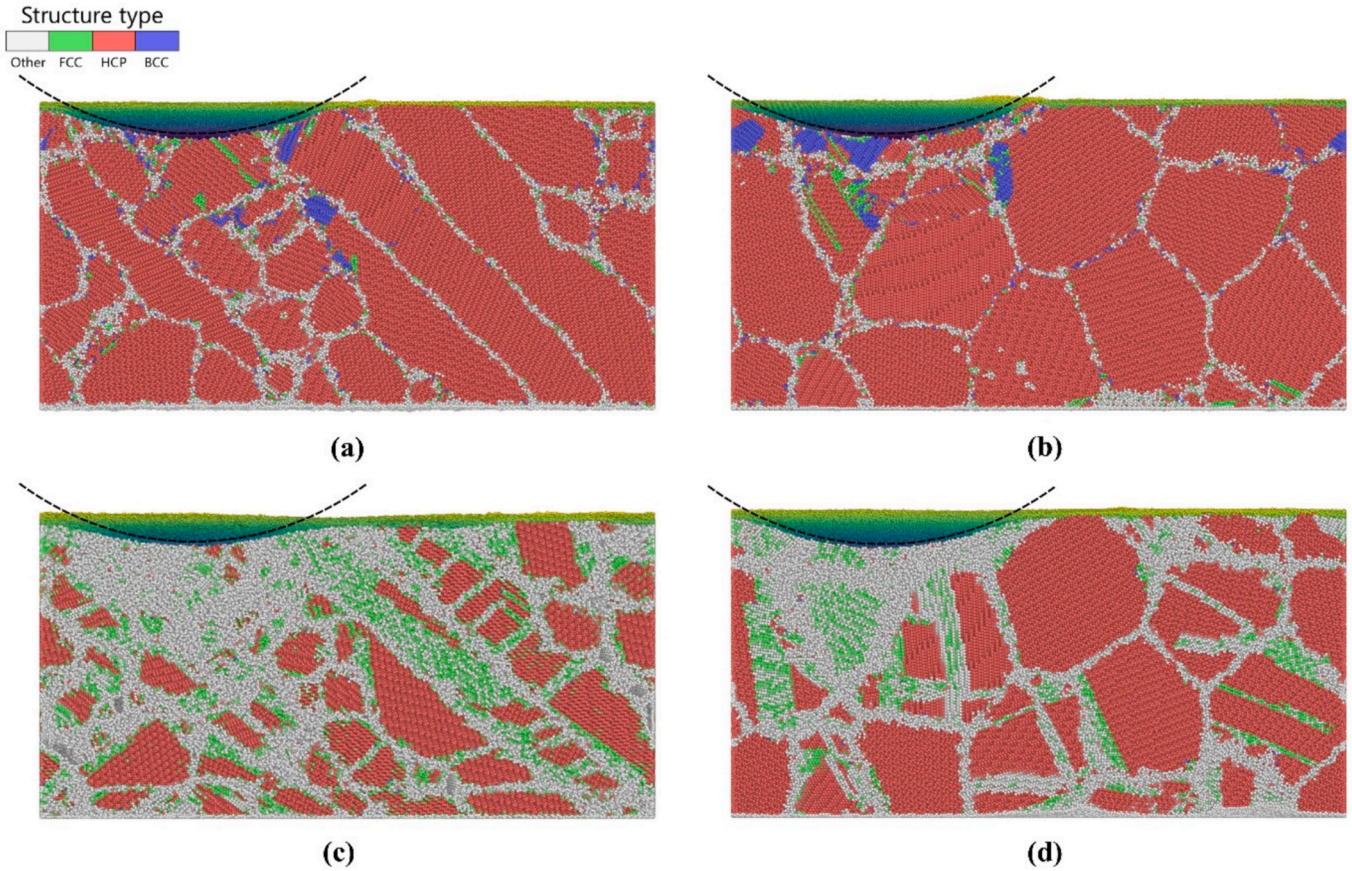


**Fig. 14.** System cross-sections of (a) acicular Ti, (b) equiaxed Ti, (c) acicular $TiN_{0.3}$, and (d) equiaxed $TiN_{0.3}$ after 0.75 ns of scratching. Atoms identified as HCP are shown in red, and atoms with undefined local structure in white. Surface atoms are colour-coded according to height (topography). Stacking faults and twinning (green) as well as BCC lattice transformations (blue) occur predominantly beneath the indenter in the Ti systems (a and b). In $TiN_{0.3}$ systems (c and d), octahedral site occupation by nitrogen (removed for clarity) results in larger plastically affected regions, with evidence of increased grain refinement and stacking fault formation. (For interpretation of the references to colour in this figure legend, the reader is referred to the web version of this article.)

causes local lattice distortions, supporting the formation of harder nitride phases and inhibiting dislocation motion, consistent with the strengthened, abrasion-resistant microstructures observed experimentally.

In contrast, argon atmospheres, being inert, do not contribute interstitial elements but influence anisotropic lattice expansion through thermal effects, resulting in smaller grain sizes and variability in elastic modulus due to texture development. The Ti Ar/Ar samples show inconsistent tribological behaviour. Areas with localised oxygen contamination reduce running-in and adhesive wear, while oxygen-poor regions suffer severe adhesive wear. This heterogeneity reflects surface reactivity differences and oxygen entrapment facilitated by finer grain structures.

The integrated experimental-computational approach confirms that interstitial oxygen and nitrogen have a significant influence on titanium's microstructural evolution and tribological performance through electronic passivation, lattice strain, and microstructural refinement mechanisms. Future research should extend the atomic-scale simulations to explore varied nitrogen and oxygen compositions, dynamic cyclic loading regimes, and multiscale modelling frameworks that bridge atomistic and continuum scales. Such investigations will deepen mechanistic understanding and guide the design of optimised titanium surfaces for demanding industrial and biomedical tribological applications.

## CRediT authorship contribution statement

**Amod Kashyap:** Writing – review & editing, Writing – original draft, Visualization, Validation, Methodology, Investigation, Formal analysis, Data curation, Conceptualization. **Hendrik J. Ehrich:** Writing – review & editing, Visualization, Validation, Investigation, Formal analysis, Data curation, Conceptualization. **Manel Rodríguez Ripoll:** Writing – review & editing, Visualization, Supervision, Resources. **Stefan J. Eder:** Writing – review & editing, Visualization, Validation, Supervision, Resources, Project administration, Funding acquisition, Data curation, Conceptualization. **Christian Greiner:** Writing – review & editing, Visualization, Validation, Supervision, Resources. **Johannes Schneider:** Writing – review & editing, Validation, Supervision, Resources, Project administration, Funding acquisition, Conceptualization.

## Declaration of competing interest

The authors declare the following financial interests/personal relationships which may be considered as potential competing interests: Stefan J Eder reports financial support was provided by Austrian Research Promotion Agency (FFG). If there are other authors, they declare that they have no known competing financial interests or personal relationships that could have appeared to influence the work reported in this paper.

## Acknowledgement

The authors would like to thank Dr. Dominic Linsler from Fraunhofer Institute for Mechanics of Materials IWM for the nano-hardness measurements. The authors would also like to thank Dr. Jens Gibmeier from the Institute for Applied Materials (IAM-WK), Karlsruhe Institute of Technology for the XRD measurements. H.J.E., M.R.R., and S.J.E. acknowledge Project K2 InTribology2, no. 906860 of the Austrian Research Promotion Agency (FFG). The computational results presented in this work were produced using the Vienna Scientific Cluster (VSC).

## Appendix A. Supplementary data

Supplementary data to this article can be found online at https://doi.org/10.1016/j.apsusc.2026.166382.

## Data availability

Data will be made available on request.

## References

[1] M.L. Kotsar, S.A. Lavrikov, V.I. Nikonov, A.V. Aleksandrov, S.G. Akhtonov, A. V. Aleksandrov, High-purity titanium, zirconium, and hafnium in nuclear power, At. Energ. 111 (2011) 92–98, https://doi.org/10.1007/s10512-011-9459-4.
[2] D. Yue, X. Jiang, H. Yu, D. Sun, In-situ fabricated hierarchical nanostructure on titanium alloy as highly stable and durable super-lubricated surface for anti-biofouling in marine engineering, Chem. Eng. J. 463 (2023) 142389, https://doi.org/10.1016/j.cej.2023.142389.
[3] A.H. Plaine, M.R. da Silva, C. Bolfarini, Tailoring the microstructure and mechanical properties of metastable Ti–29Nb–13Ta-4.6Zr alloy for self-expansible stent applications, J. Alloys Compd. 800 (2019) 35–40, https://doi.org/10.1016/j.jallcom.2019.06.049.
[4] K. Ronoh, F. Mwema, S. Dabees, D. Sobola, Advances in sustainable grinding of different types of the titanium biomaterials for medical applications: a review, Biomed. Eng. Adv. 4 (2022) 100047, https://doi.org/10.1016/j.bea.2022.100047.
[5] Y. Jia, W. Zeng, Z. Fan, Q. Meng, H. Liu, Y. Peng, An effective titanium salt dosing strategy for phosphorus removal from wastewater: synergistic enhancement of chemical and biological treatment, Sci. Total Environ. 842 (2022) 156960, https://doi.org/10.1016/j.scitotenv.2022.156960.
[6] J. Kaspar, J. Bretschneider, S. Jacob, S. Bonß, B. Winderlich, B. Brenner, Microstructure, hardness and cavitation erosion behaviour of Ti-6Al-4V laser nitrided under different gas atmospheres, Surf. Eng. 23 (2007) 99–106, https://doi.org/10.1179/174329407X169430.
[7] H. Mohseni, P. Nandwana, A. Tsoi, R. Banerjee, T.W. Scharf, In situ nitrided titanium alloys: microstructural evolution during solidification and wear, Acta Mater. 83 (2015) 61–74, https://doi.org/10.1016/j.actamat.2014.09.026.
[8] F.B. Kværndrup, Ö.C. Kücükyildiz, G. Winther, M.A.J. Somers, T.L. Christiansen, Extreme hardening of titanium with colossal interstitial contents of nitrogen and oxygen, Mater. Sci. Eng. A 813 (2021), https://doi.org/10.1016/j.msea.2021.141033.
[9] J.D.C. Tardelli, M.A. Schiavon, A.C. dos Reis, Chitosan coatings on titanium-based implants - from development to characterization and behavior: a systematic review, Carbohydr. Polym. 344 (2024) 122496, https://doi.org/10.1016/j.carbpol.2024.122496.
[10] H. Dong, T. Bell, Enhanced wear resistance of titanium surfaces by a new thermal oxidation treatment, Wear 238 (2000) 131–137, https://doi.org/10.1016/S0043-1648(99)00359-2.
[11] D. Kümmel, J. Schneider, P. Gumbsch, Influence of interstitial oxygen on the tribology of Ti6Al4V, Tribol. Lett. 68 (2020), https://doi.org/10.1007/s11249-020-01327-4.
[12] D. Kümmel, M. Hamann-Schroer, H. Hetzner, J. Schneider, Tribological behavior of nanosecond-laser surface textured Ti6Al4V, Wear 422–423 (2019) 261–268, https://doi.org/10.1016/j.wear.2019.01.079.
[13] Z. Chen, Z. Wang, J. Liu, Z. Ye, Y. Hu, J. Wu, K. Liu, Z. Cai, Enhancing the tribological properties of TA1 pure titanium by modulating the energy of pulsed laser nitriding, Opt. Laser Technol. 169 (2024) 110118, https://doi.org/10.1016/j.optlastec.2023.110118.
[14] M.P. Kapczinski, E.J. Kinast, C.A. dos Santos, Near-surface composition and tribological behaviour of plasma nitrided titanium, J. Phys. D Appl. Phys. 36 (2003) 1858, https://doi.org/10.1088/0022-3727/36/15/317.
[15] B. Zhang, Q. Dong, Z. Ba, Z. Wang, H. Shi, Y. Xue, Tribological properties of surface-textured and plasma-nitrided pure titanium under oil lubrication condition, J. Mater. Eng. Perform. 27 (2018) 186–193, https://doi.org/10.1007/s11665-017-3100-1.
[16] G. Cassar, S. Banfield, J.-C.-A.-B. Wilson, J. Housden, A. Matthews, A. Leyland, Tribological properties of duplex plasma oxidised, nitrided and PVD coated Ti–6Al–4V, Surf. Coat. Technol. 206 (2011) 395–404, https://doi.org/10.1016/j.surfcoat.2011.07.037.
[17] D. She, W. Yue, Z. Fu, C. Wang, X. Yang, J. Liu, Effects of nitriding temperature on microstructures and vacuum tribological properties of plasma-nitrided titanium, Surf. Coat. Technol. 264 (2015) 32–40, https://doi.org/10.1016/j.surfcoat.2015.01.029.
[18] D. Kümmel, D. Linsler, R. Schneider, J. Schneider, Surface engineering of a titanium alloy for tribological applications by nanosecond-pulsed laser, Tribol. Int. 150 (2020), https://doi.org/10.1016/j.triboint.2020.106376.
[19] J.L. Sun, P.W. Trimby, F.K. Yan, X.Z. Liao, N.R. Tao, J.T. Wang, Grain size effect on deformation twinning propensity in ultrafine-grained hexagonal close-packed titanium, Scr. Mater. 69 (2013) 428–431, https://doi.org/10.1016/j.scriptamat.2013.06.001.
[20] Z. Zou, M. Simonelli, J. Katrib, G. Dimitrakis, R. Hague, Refinement of the grain structure of additive manufactured titanium alloys via epitaxial recrystallization enabled by rapid heat treatment, Scr. Mater. 180 (2020) 66–70, https://doi.org/10.1016/j.scriptamat.2020.01.027.
[21] P. Wang, X. Tan, M.L.S. Nai, J. Wu, J. Wei, Deformation induced nanoscale twinning improves strength and ductility in additively manufactured titanium alloys, Mater. Sci. Eng. A 833 (2022), https://doi.org/10.1016/j.msea.2021.142568.
[22] K. Li, X. Liu, Y. Liu, X. Wu, W. Zhang, J. Yang, W. Li, S. Zhou, Strengthening layer with nano-twins in titanium alloy induced by laser surface re-melting: mechanism

of high strength and ductility, Mater Charact 196 (2023), https://doi.org/10.1016/j.matchar.2022.112632.
[23] A.M. Ventura Cervellón, M. Varga, M. Rodríguez Ripoll, S.J. Eder, Resolving high-strain-rate scratch behavior of $Ti_6Al4_V$ in experiment and meshless simulation, Wear 558–559 (2024) 205554, https://doi.org/10.1016/j.wear.2024.205554.
[24] C.M. Yang, X.B. Liu, Z.X. Zhu, A. Zhou, H. Bin Zhou, S.H. Zhang, Study of tribological property of laser-cladded FeCoCrNiMnx high-entropy alloy coatings via experiment and molecular dynamics simulation, Tribol. Int. 191 (2024), https://doi.org/10.1016/j.triboint.2023.109106.
[25] V.K. Balla, J. Soderlind, S. Bose, A. Bandyopadhyay, Microstructure, mechanical and wear properties of laser surface melted $Ti_6Al_4V$ alloy, J. Mech. Behav. Biomed. Mater. 32 (2014) 335–344, https://doi.org/10.1016/j.jmbbm.2013.12.001.
[26] W.C. Oliver, G.M. Pharr, I. Introduction, An improved technique for determining hardness and elastic modulus using load and displacement sensing indentation experiments W, J. Mater. Res. 7 (1992) 1564–1583.
[27] M.A. Groeber, M.A. Jackson, DREAM.3D: a digital representation environment for the analysis of microstructure in 3D, Integr. Mater. Manuf. Innov. 3 (2014) 56–72, https://doi.org/10.1186/2193-9772-3-5.
[28] A.P. Thompson, H.M. Aktulga, R. Berger, D.S. Bolintineanu, W.M. Brown, P. S. Crozier, P.J. in 't Veld, A. Kohlmeyer, S.G. Moore, T.D. Nguyen, R. Shan, M. J. Stevens, J. Tranchida, C. Trott, S.J. Plimpton, LAMMPS - a flexible simulation tool for particle-based materials modeling at the atomic, meso, and continuum scales, Comput. Phys. Commun. 271 (2022) 108171, https://doi.org/10.1016/j.cpc.2021.108171.
[29] Y.-K. Kim, H.-K. Kim, W.-S. Jung, B.-J. Lee, Atomistic modeling of the Ti–Al binary system, Comput. Mater. Sci 119 (2016) 1–8, https://doi.org/10.1016/j.commatsci.2016.03.038.
[30] Y.-M. Kim, B.-J. Lee, Modified embedded-atom method interatomic potentials for the Ti–C and Ti–N binary systems, Acta Mater. 56 (2008) 3481–3489, https://doi.org/10.1016/j.actamat.2008.03.027.
[31] P.M. Larsen, S. Schmidt, J. SchiØtz, Robust structural identification via polyhedral template matching, Model. Simul. Mat. Sci. Eng. 24 (2016), https://doi.org/10.1088/0965-0393/24/5/055007.
[32] D.W. Wang, Y.H. Zhou, J. Shen, Y. Liu, D.F. Li, Q. Zhou, G. Sha, P. Xu, T. Ebel, M. Yan, Selective laser melting under the reactive atmosphere: a convenient and efficient approach to fabricate ultrahigh strength commercially pure titanium without sacrificing ductility, Mater. Sci. Eng. A 762 (2019) 138078, https://doi.org/10.1016/j.msea.2019.138078.
[33] X. Zong, H. Wang, J. Li, X. Cheng, Z. Li, H. Tang, Microstructure characterization and evolution mechanism of titanium during laser surface nitriding, Mater Charact 190 (2022), https://doi.org/10.1016/j.matchar.2022.112029.
[34] W. Wu, G. Xie, L. Sun, Y. Yang, H. Hong, S. Zhang, D. Li, A study on adsorption, dissociation, penetration, and diffusion of nitrogen on and in α-Ti via First-principles calculations, Vacuum 221 (2024), https://doi.org/10.1016/j.vacuum.2023.112856.
[35] Y.S. Zhang, Y.H. Zhao, W. Zhang, J.W. Lu, J.J. Hu, W.T. Huo, P.X. Zhang, Core-shell structured titanium-nitrogen alloys with high strength, high thermal stability and good plasticity, Sci. Rep. 7 (2017), https://doi.org/10.1038/srep40039.
[36] C.-W. Chan, S. Lee, G.C. Smith, C. Donaghy, Fibre laser nitriding of titanium and its alloy in open atmosphere for orthopaedic implant applications: investigations on surface quality, microstructure and tribological properties, Surf. Coat. Technol. 309 (2017) 628–640, https://doi.org/10.1016/j.surfcoat.2016.12.036.
[37] N. Vaché, Y. Cadoret, B. Dod, D. Monceau, Modeling the oxidation kinetics of titanium alloys: review, method and application to Ti-64 and Ti-6242s alloys, Corros. Sci. 178 (2021) 109041, https://doi.org/10.1016/j.corsci.2020.109041.
[38] H. Okamoto, O-Ti (oxygen-titanium), J. Phase Equilibria Diffus. 32 (2011) 473–474, https://doi.org/10.1007/s11669-011-9935-5.
[39] A.V. Ruban, V.I. Baykov, B. Johansson, V.V. Dmitriev, M.S. Blanter, Oxygen and nitrogen interstitial ordering in hcp Ti, Zr, and Hf: an ab initio study, Phys. Rev. B: Condens. Matter Mater. Phys. 82 (2010), https://doi.org/10.1103/PhysRevB.82.134110.
[40] E. Chikarakara, S. Naher, D. Brabazon, High speed laser surface modification of Ti–6Al–4V, Surf. Coat. Technol. 206 (2012) 3223–3229, https://doi.org/10.1016/j.surfcoat.2012.01.010.
[41] S.R. Nishitani, S. Yoshimura, H. Kawata, M. Yamaguchi, Deposition of nitrides and oxides of aluminum and titanium by pulse laser irradiation, J. Mater. Res. 7 (1992) 725–733, https://doi.org/10.1557/JMR.1992.0725.
[42] A.M. Kamat, S.M. Copley, A.E. Segall, J.A. Todd, Laser-sustained plasma (LSP) nitriding of titanium: a review, Coatings 9 (2019), https://doi.org/10.3390/coatings9050283.
[43] X. Zong, H. Wang, H. Tang, X. Cheng, X. Tian, X. Ran, Microstructure evolution and mass transfer behavior during multi-pass laser surface nitriding process on titanium alloy, Surf. Coat. Technol. 466 (2023), https://doi.org/10.1016/j.surfcoat.2023.129565.
[44] C.R. LaRosa, M. Shih, C. Varvenne, M. Ghazisaeidi, Solid solution strengthening theories of high-entropy alloys, Mater Charact 151 (2019) 310–317, https://doi.org/10.1016/j.matchar.2019.02.034.